Time-resolved spectroscopic study of photofragment fluorescence in methane/air mixtures and its diagnostic implications

Malin Jonsson[1] · Jesper Borggren[1] · Marcus Aldén[1] · Joakim Bood[1]

Abstract In this work 80-picosecond laser pulses of 266-nm wavelength with intensities up to $(2.0 \pm 0.5) \times 10^{11}$ W/cm^2 were used for fragmentation of methane/air gas mixtures at ambient pressure and temperature. Emission spectra are, for the first time, studied with ultrahigh temporal resolution using a streak camera. Fluorescence spectra from CH($A^2\Delta$–$X^2\Pi$, $B^2\Sigma^-$–$X^2\Pi$, $C^2\Sigma^+$–$X^2\Pi$), CN($B^2\Sigma^+$–$X^2\Sigma^+$, $\Delta v = 0$ and $\Delta v = \pm 1$), NH($A^3\Pi^-$–$X^3\Sigma^-$), OH($A^2\Sigma^+$–$X^2\Pi$) and N$_2^+$($B^2\Sigma_u^+$–$X^2\Sigma_g^+$) were recorded and analyzed. By fitting simulated spectra to high-resolution experimental spectra, rotational and vibrational temperatures are estimated, showing that CH(C), CN(B), NH(A), and OH(A) are formed in highly excited vibrational and rotational states. The fluorescence signal dependencies on laser intensity and CH$_4$/air equivalence ratio were investigated as well as the fluorescence lifetimes. All fragments observed are formed within 200 ps after the arrival of the laser pulse and their fluorescence lifetimes are shorter than 1 ns, except for CN(B–X) $\Delta v = 0$ whose lifetime is 2.0 ns. The CN(B–X) $\Delta v = 0$ fluorescence was studied temporally under high spectral resolution, and it was found that the vibrational levels are not populated simultaneously, but with a rate that decreases with increasing vibrational quantum number. This observation indicates that the rate of the chemical reaction that forms the CN(B) fragments is decreasing with increasing vibrational state of the product. The results provide vital information for the application of laser diagnostic techniques based on strong UV excitation, as they show that such methods might not be entirely non-intrusive and suffering from spectral interferences, unless the laser intensity is kept sufficiently low. Finally, equivalence ratios were determined from "unknown" spectra using multivariate analysis, showing a good agreement with theoretical compositions with an error of 4 %. The method is expected to be a useful diagnostic tool for measurements of local equivalence ratios in for example combustion environments.

1 Introduction

The interaction of intense laser light with matter and especially the influence of lasers on molecular processes such as dissociation and ionization have received attention across different research fields, see for example [1] and references therein. The photodissociation and ionization processes of methane (CH$_4$) and other hydrocarbons have been the focus of a number of studies, e.g., [2–7]. Methane is particularly interesting since it is the main component in natural gas, but also the most abundant hydrocarbon on earth, and therefore an important atmospheric trace species and a greenhouse gas [8–11]. Hence, the possibility to measure concentrations of methane is of vital importance for understanding atmospheric and combustion chemistry, especially in biofuel combustion.

Photodissociation dynamics of molecules has mostly been investigated by use of low-intensity light sources ($<10^{10}$ W/cm^2), such as conventional UV lamps or weak nanosecond laser pulses in the UV regime. Using low-intensity light sources leads to photodissociation through a single-photon absorption process. Extensive research on

✉ Malin Jonsson
malin.jonsson@forbrf.lth.se

[1] Division of Combustion Physics, Department of Physics, Lund University, Box 118, 221 00 Lund, Sweden

photodissociation dynamics based on single-photon photolysis has been described and discussed in several review articles and text books, see, e.g., [12–14]. During the last decade, however, extremely intense femtosecond laser pulses ($>10^{13}$ W/cm^2) have been used for spectroscopic studies of ionization and dissociation processes in several hydrocarbons, especially methane [15–21]. These studies show that the dissociation processes are completely different for weak and strong laser photolysis. As mentioned previously, a weak light source results in single-photon excitation to low-lying repulsive electronic states and implies that typically only one or two bonds in the parent molecule are broken. In contrast, photolysis using ultra-intense light sources results in multi-photon excitation to high-lying dissociative states, which causes breakage of multiple bonds, and the creation of a multitude of photofragments [15].

In addition to multi-photon dissociation, ultra-short laser pulses may cause optical breakdown of the gaseous medium due to multi-photon ionization processes, which leads to plasma formation. This phenomenon is used for diagnostic purposes in laser-induced breakdown spectroscopy (LIBS), see, e.g., [22] for a comprehensive review of diagnostic aspects and [23] for a review of the current state-of-the-art of LIBS diagnostics with numerous application examples. Recently, Kotzagianni and Couris reported studies of femtosecond LIBS in CH$_4$/air flames [18, 20] and in various CH$_4$/N$_2$ mixtures at room temperature [20]. They found that the emission corresponding to the B$^2\Sigma^+$–X$^2\Sigma^+$ $\Delta v = 0$ band of CN is the most intense spectral feature and that it is linearly dependent on the CH$_4$ concentration, allowing for determination of local equivalence ratio in the flame. Excited molecular fragments can also be created by the high intensity prevailing inside a laser filament. For high enough peak power, such a filament can easily be produced by a femtosecond laser as the beam undergoes self-focusing due to the intensity dependence of the refractive index, creating a plasma, which in turn defocuses the beam. In this way the beam is repeatedly self-focused/defocused and the dynamic balance between these two mechanisms results in the propagation of laser light in a very thin (d ~100 μm) self-sustained channel, a so-called laser filament [24]. Several papers report on fluorescent fragments of methane and other hydrocarbons induced by femtosecond laser filament excitation [17–21].

In multi-photon dissociation associated to both LIBS and filamentation, spectral lines from ions and excited atomic fragments occur in the emission spectrum. In addition, the spectrum typically contains a broadband continuum due to bremsstrahlung or, in the filamentation case, self-phase modulation. In the work by Kong et al. [15], it is shown that it is possible to perform multi-photon dissociation in methane, ethylene, n-butane, and 1-butene, using an ultra-intense femtosecond laser pulse (2×10^{14} W/cm^2),

resulting in emission from only neutral fragments. They conclude that the fragmentation process in their study cannot be due to Coloumb explosion of multiply charged ions, but instead should be explained as a multiple-channel dissociation of the super-excited state of the parent molecule [15].

In the present work, we have investigated emission spectra resulting from dissociation, induced by a focused 266-nm picosecond pulse of intermediate intensity (2.0×10^{11} W/cm^2), in different mixtures of methane and air at room temperature and atmospheric pressure. The laser intensity is kept below the threshold for plasma formation, i.e., neither breakdown or filamentation occur. A streak camera is used behind a spectrograph, providing 2-dimensional fluorescence maps with time and wavelength along the horizontal and vertical axis, respectively, which thus allows spectroscopic analysis with outstanding temporal resolution. The implication of the findings based on diagnostics with strong UV laser excitation is discussed in the final section, where also a novel concept, based on multivariate analysis, is demonstrated for determination of equivalence ratio.

2 Experimental setup

Intense picosecond laser pulses are generated from a mode-locked Nd:YAG laser (Ekspla, PL-2143C) that provides pulses of 80-ps duration and 10-Hz pulse repetition rate. The fundamental output at 1064 nm is frequency quadrupled, providing pulses with a wavelength of 266 nm having a full width at half maximum (FWHM) of 2 cm^{-1}. The laser beam was focused by a 300-mm focal length spherical lens into the measurement volume located above a vertical tube, containing a free flow of methane and air of different proportions. The laser pulse energy was ~2.5 mJ, and the laser beam waist had a diameter of 140 μm, resulting in a laser pulse intensity of 2.0×10^{11} W/cm^2 in the probe volume, with an uncertainty of $\pm 0.5 \times 10^{11}$ W/cm^2. The total gas flow was 10 l/min and was regulated with calibrated mass flow controllers. For spectral investigation, the fluorescence signal was collected by two spherical lenses; +50 and +200 mm focal length, perpendicular to the measurement volume and imaged onto the entrance slit of a 0.5-m spectrograph (Princeton Instruments, Acton Model SP-2556) equipped with an intensified CCD camera (Princeton Instruments, PIMAX III). Two different gratings were used in the spectrograph; either one with 150 grooves/mm or one with 1200 grooves/mm. The latter grating provided a spectral resolution of 0.12 nm with a slit width of 50 μm. The CCD camera was synchronized with the laser, and the image intensifier was gated, capturing light within a temporal window of 100 ns succeeding the arrival of the

laser pulse. The two lenses used for signal collection, mentioned above, imply four times magnification of the probe volume. The diameter of the laser beam at its focus will thus appear with a diameter of 560 μm in the image on the horizontal slit. Since the horizontal slit of the spectrograph had a width of 50 μm, only signal induced from a narrow plane in the middle of the laser beam was collected, which, to some extent, reduces the impact of spatial laser intensity variations.

For time-resolved spectral studies, the fluorescence signal was imaged onto the entrance slit of a spectrograph (Spectral Products, Digikröm DK 240) connected to a streak camera (Optronis, Optoscope). This detection system thus generates images with wavelength on one axis and time on the other axis, which makes it possible to investigate molecular dissociation and formation in great detail. The horizontal slit of the streak camera, located in the focal plane of the spectrograph, had a width of 400 μm, while the vertical entrance slit of the spectrograph had a width of 15 μm. Two different spectrometer gratings were used, one with a 150 grooves/mm grating and one with 2400 grooves/mm, the latter providing a spectral resolution of 0.5 nm. For all measurements, a liquid *N,N*-dimethylformamide absorption filter was positioned in front of the spectrographs to suppress scattered laser light.

3 Results and discussion

3.1 Spectral assignments

The fluorescence emitted by fragments created by a picosecond laser pulse, having an intensity of approximately 2.0×10^{11} W/cm^2, was recorded spectrally dispersed using a spectrometer coupled to a gated CCD camera. Figure 1 shows a fluorescence spectrum recorded in a free gas flow of a stoichiometric mixture of methane and air. The data were accumulated over 500 laser shots. The spectral lines correspond to fluorescence of the electronically excited free radicals; CN, CH, NH, and ionized molecular nitrogen N_2^+. Raman scattering from O_2, N_2, and CH_4 is also visible in the spectrum. The red spectra represent emission features recorded with high spectral resolution. It is clear from the figure that the spectral features at 358, 388 and 418 nm correspond to different vibrational bands, $\Delta v = -1$, 0, and $+1$, respectively, of the $B^2\Sigma^+–X^2\Sigma^+$ transition in CN. Furthermore, the spectral structures at 314 and 430 nm are assigned to the $C^2\Sigma^+–X^2\Pi$ and $A^2\Delta–X^2\Pi$, respectively, transitions in CH. The CH fluorescence of the $B^2\Sigma^-–X^2\Pi$ transition, R-branch band head at 387 nm, is superimposed on the strong $\Delta v = 0$ band of CN(B–X) at 388 nm and the $B^2\Sigma_u^+–X^2\Sigma_g^+$ fluorescence (0–0 band) of N_2^+ at 391 nm, and can therefore not be further analyzed. The peaks at 336
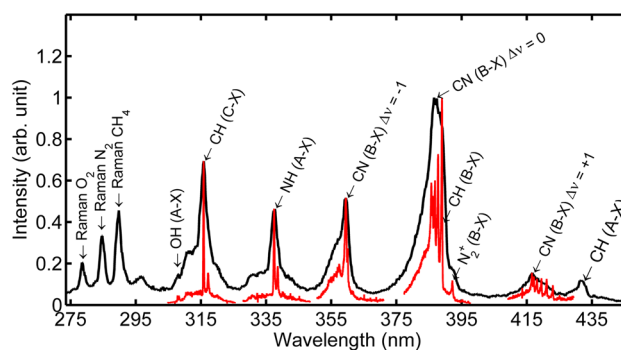

Fig. 1 Low-resolution emission spectrum (*black*) induced by intense 80-picosecond laser pulses. The spectrum is based on an accumulation of 500 laser shots. The identified fragments and associated transitions are denoted in figure. The red spectra were recorded with the high-resolution grating in the spectrograph

and 337 nm correspond to the (0,0) and (1,1) band, respectively, of the $(A^3\Pi–X^3\Sigma^-)$ system in NH, and finally, the low peak at 309 nm is due to emission corresponding to the (0,0) band of $OH(A^2\Sigma^+–X^2\Pi)$.

It is noteworthy that the spectrum shown in Fig. 1 does not contain any spectral features from atoms, e.g., H, O, C, and N, and the background level is low. It should also be mentioned that the grating of the spectrograph was rotated to get access to the spectral range 430–650 nm in order to investigate whether C_2 fragments were produced. However, no spectral features reminiscent of the C_2 Swan band were observed. A comparison between the low-(black) and high-resolution (red) spectrum shows that the background level in the low-resolution spectrum is mainly due to the limited spectral resolution. Furthermore, no spark, i.e., white-light emission indicative of breakdown and plasma formation, was visible in the laser beam focus. These observations indicate no or very little plasma formation, yet highly excited molecular fragments are created.

3.2 Comparisons with simulated spectra

The fact that fragments are created in electronically excited states means that significant excess energy is available in the fragmentation process. The shapes of the high-resolution spectra, i.e., the red curves in Fig. 1, indicate that there is sufficient excess energy to even cause significant rotational and vibrational excitation of the fragments. In order to further examine these properties, the experimental spectra were compared with simulated spectra. Fluorescence spectra corresponding to CH(C–X), OH(A–X), and CN(B–X) were simulated using the software LIFBASE [25], while NH(A–X) fluorescence was simulated with PGOPHER [26] using molecular constants from [27]. The simulated spectra were fitted to the measured spectra with rotational and vibrational temperature as fitting parameters, i.e., both rotational and
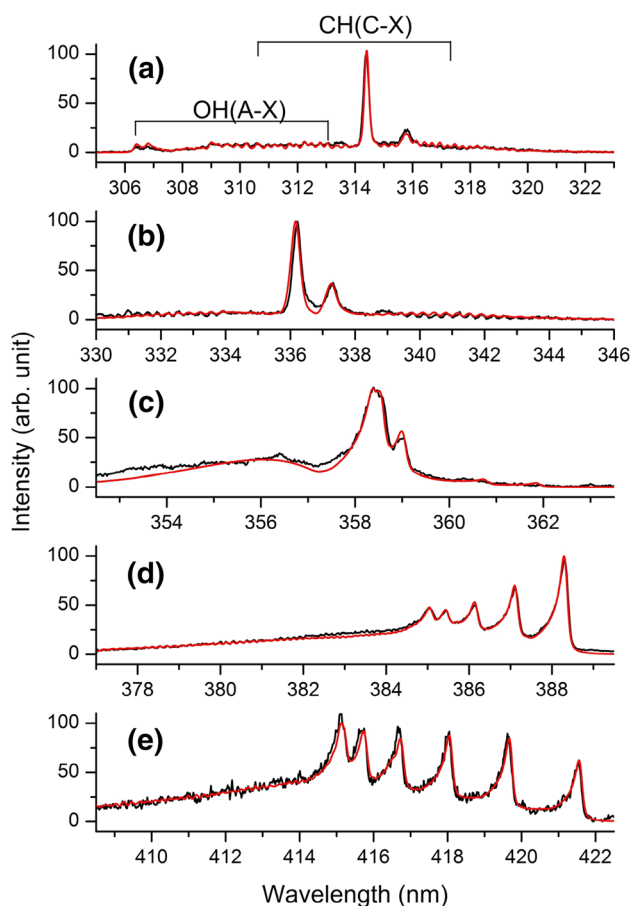
Fig. 2 Experimental (*black*) and best-fit simulated (*red*) spectra of fluorescence corresponding to CH(C–X) and OH(A–X) (**a**), NH(A–X) (**b**), CN(B–X) $\Delta v = -1$ (**c**), CN(B–X) $\Delta v = 0$ (**d**), and CN(B–X) $\Delta v = +1$ (**e**)

Table 1 Vibrational and rotational temperatures determined by fitting simulated fluorescence spectra to experimental data recorded in a stoichiometric mixture of methane and air at 296 K

Spectral feature	Vibrational temperature (K)	Rotational temperature (K)
CN(B–X) $\Delta v = 0$	7000 ± 1000	7000 ± 1000
CN(B–X) $\Delta v = -1$	8000 ± 1000	4500 ± 500
CN(B–X) $\Delta v = +1$	8000 ± 1000	6500 ± 1000
CH(C–X)	3000 ± 500	2000 ± 500
NH(A–X)	*	3000 ± 500
OH(A–X)	5000 ± 2000	5000 ± 2000

vibrational populations were kept Boltzmann distributed in the fits. Figure 2 displays experimental and best-fit simulated spectra, while Table 1 summarizes the results in terms of vibrational and rotational temperatures corresponding to the best-fit spectra. Due to the presence of a nitrogen emission line, namely the 0–0 band of $N_2(C^3\Pi_u – B^3\Pi_g)$ at 337 nm [28], which interferes with the first hot-band of NH(A–X), no vibrational temperature was evaluated for NH(A–X).

It should be noted that the recorded emission spectra reflect the vibrational/rotational population distributions corresponding to the time-integrated fluorescence signal, i.e., not the nascent distributions. Hence, the spectra are affected by vibrational (VET) and rotational energy transfer (RET) processes due to collisions. This means that vibrational and rotational temperatures of the nascent temperatures are expected to be higher than the temperatures reported here. The deviation from the nascent temperature is strongly dependent on the fluorescence lifetimes, such that shorter lifetimes mean less impact from VET and RET and vice versa.

As can be seen in Fig. 2, the best-fit spectra generally agree well with the corresponding measured spectra. One possible reason for the slight deviation between measured and fitted spectrum for the $\Delta v = -1$ band of CN(B–X), shown in panel (c), is interfering fluorescence from N_2^+(B–X), whose $\Delta v = +1$ band has its band heads near 358 nm. Since a signal from N_2^+(B–X) $\Delta v = 0$ is observed at 391 nm, as shown in Fig. 1, fluorescence in the $\Delta v = +1$ is of course a possibility. The fact that the difference between the experimental and fitted CN(B–X) $\Delta v = +1$ spectrum is small, however, suggests that the N_2^+(B–X) $\Delta v = +1$ fluorescence is very weak.

Fluorescence from N_2^+ may also be the reason for the very small discrepancy, near 390 nm, between measured and fitted spectrum for CN(B–X) $\Delta v = 0$, shown in panel (d), since N_2^+(B–X) $\Delta v = 0$ has its band heads at ~391 nm and that the bands are blue-shaded. The fact that the fitted spectra generally agree well with the experimental data suggest that the vibrational and rotational populations of the electronically excited fragments are Boltzmann distributed.

As can be seen in Table 1, all observed fragments have very high vibrational and rotational temperatures, indicating that significant excess energy ends up in vibrational and rotational energy of the fragments. The CN(B) fragments show the highest vibrational and rotational temperatures. The emission bands corresponding to $\Delta v = 0, -1$, and $+1$ should reflect the same vibrational and rotational populations in CN(B), yet the rotational temperature extracted from the $\Delta v = -1$ is significantly lower than for the other two bands, 4500 K in comparison with 7000 and 6500 K for $\Delta v = 0$ and $+1$, respectively. One possible reason for this discrepancy might be the aforementioned interfering fluorescence from N_2^+(B–X), $\Delta v = +1$. NH(A) and OH(A) have the same vibrational temperature, 5000 K, but the rotational temperatures are different; 5000 K for OH(A) and 3000 K for NH(A). The OH(A) temperatures are, however, more uncertain than the NH(A) temperatures because of two reasons: The OH(A–X) spectrum is much weaker

than the NH(A–X) spectrum, as can be seen in Fig. 1, and there is considerable crosstalk between the OH(A–X) spectrum and the significantly stronger CH(C–X) spectrum, as shown in Fig. 2a.

As reported in Table 1, the CH(C) temperatures are significantly lower than the temperatures of the other investigated species, both in terms of vibration and rotation. It should be noted that CH is the only fragment of those studied here that can be formed directly through photodissociation of a single species, whereas formation of the other fragments requires a chemical reaction. This circumstance suggests that the chemical reactions involved in producing OH, NH, and, in particular, CN, should be highly exothermic. Possible formation channels for vibrationally and rotationally excited CN(B) are $C_2 + N_2 \rightarrow 2CN$, $C + N_2 \rightarrow CN + N$, and $C^+ + N_2 \rightarrow N^+ + CN$ [20].

Kong et al. [15], who studied fragments produced by intense femtosecond laser pulses (2×10^{14} W/cm^2) of 800 nm wavelength in pure methane, suggest that the only dissociation pathway that creates vibrationally and rotationally excited CH* is through CH_2, via $CH_2 \rightarrow CH^* + H$, where CH_2 is formed by dissociation of methane, e.g., via $CH_4 \rightarrow CH_2 + H_2$ or $CH_4 \rightarrow CH_2 + 2H$, where the first process is most energetically favorable [15, 29, 30]. They found that the CH(C) fragments had a vibrational temperature of 1200 ± 300 K and a rotational temperature of 1100 ± 500 K, which are significantly lower than the corresponding temperatures determined in the present study, i.e., 3000 ± 500 K and 2000 ± 500 K, respectively. Since our result is based on a fluorescence spectrum recorded in a stoichiometric mixture of methane and air, i.e., 17.3 % CH_4, 17.3 % O_2, and 65.3 % N_2, one possible reason for our higher temperatures could be that CH(C) here to some extent is formed by exothermic chemical reactions with species originating from N_2 and O_2.

3.3 Laser intensity dependence study

The laser intensity dependence of the emission spectrum was investigated by recording spectra, using the low-resolution grating, for different laser pulse energies. The resulting spectra are not shown here, but can be found in the supplementary material (Fig. S1). The recorded data were analyzed by plotting the peak intensity of each spectral feature versus laser pulse energy in a log–log diagram. A linear function was then fitted to each data set, whereupon the slope of each fitted curve was documented, see Table 2. Figure 3 shows intensity dependence plots for four spectral features, namely CH_4 Raman scattering, CH(C–X) fluorescence, CN(B–X) $\Delta v = -1$ fluorescence, and NH(A–X) fluorescence.

As indicated in Table 2, the three Raman lines have slopes close to unity, indicating linear laser intensity

Table 2 Result of the laser intensity dependence study: spectral feature, wavelength at the highest signal intensity, and slope extracted from log–log plot

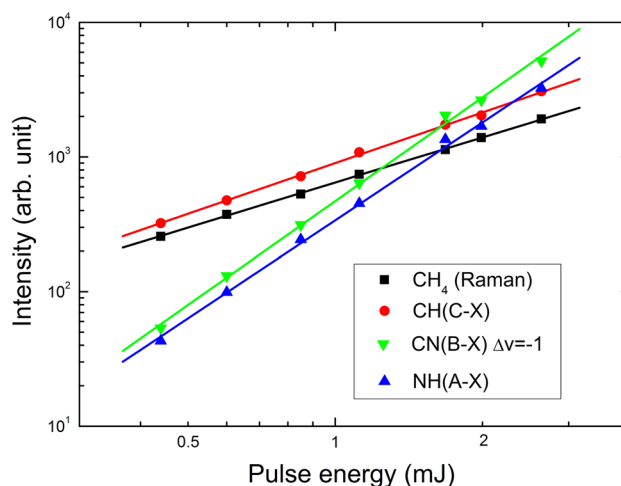| Spectral feature	Wavelength (nm)	Slope
O_2 Raman	277.4	1.2
N_2 Raman	283.5	1.2
CH_4 Raman	288.5	1.1
CH(C–X)	314.6	1.2
NH(A–X)	336.2	2.4
CN(B–X) $\Delta v = -1$	358.5	2.6
CN(B–X) $\Delta v = 0$	385.5	2.7
CN(B–X) $\Delta v = +1$	415.4	2.4
CH(A–X)	430.7	0.9

Fig. 3 Signal intensity vs laser pulse energy for four different spectral lines. The *solid lines* are linear fits to the experimental data

dependence as expected. The deviation from unity is within the experimental uncertainty of the current data. The slopes corresponding to the CH emission are close to unity too, i.e., these emission lines are also linearly dependent on the laser intensity. As can be seen in Fig. 3, the slope corresponding to CH(C–X) is very close to the slope associated with the CH_4 Raman scattering. The slopes of NH(A–X) and the three CN(B–X) bands are between 2.4 and 2.7.

The fact that the CH fluorescence is linearly dependent on laser intensity does not necessarily reflect a single-photon absorption process. In fact, such a result is very unlikely given the high laser intensities used, ranging from 3×10^{10} W/cm^2 to 2.0×10^{11} W/cm^2, with which multiphoton processes are readily accomplished. One possible path of CH(A, B, C) formation is via a super-excited state (SES), i.e., a state located above the ionization potential (IP), followed by a fast neutral dissociation (ND) into excited CH fragments [15, 31] see Fig. 4. The ionization potential of
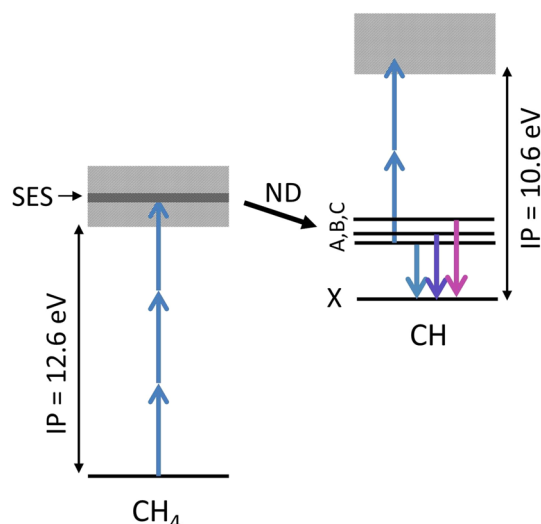
Fig. 4 Schematic illustration of how CH(A, B, C–X) fluorescence is induced via a 3-photon excitation to a super-excited state (SES), beyond the ionization potential (IP) of CH$_4$, followed by rapid neutral dissociation (ND) into CH(A, B, C) fragments. The CH(A, B, C) states are depopulated via spontaneous emission (fluorescence) and 2-photon ionization

CH$_4$ is 12.6 eV [32], which means that three 266-nm photons (14.0 eV) are needed to reach an SES above the IP. The excited CH states are located 12.2 eV (A$^2\Delta$), 12.8 eV (B$^2\Sigma^-$), and 13.3 eV (C$^2\Sigma^+$) above the ground state of CH$_4$ [15], i.e., all reachable with three 266-nm photons. Azarm et al. have investigated the dynamics of the SES and they measured a lifetime of 160 fs [31], i.e., the neutral dissociation (ND) process is extremely fast. Now, our measured laser intensity dependence of the CH fluorescence (slopes 1.2 and 0.9) indicates that the 3-photon process needed to reach the SES and finally CH(A, B, C) must occur in competition with intensity-dependent processes that counteracts formation of CH(A, B, C). The energies of CH(A), CH(B), and CH(C) are 2.9, 3.2, and 3.9 eV, respectively, above the ground state of CH. Since the IP for CH is 10.6 eV, CH(A, B, C) can be photoionized/photodissociated with two 266-nm photons (9.3 eV), as schematically illustrated in Fig. 4. Thus, one possible explanation for the observed intensity dependence of the CH fluorescence, which is close to linear, could be the combination of a 3-photon production term and a 2-photon consumption term.

Kato et al. [33] have studied super-excited states of CH$_4$ by recording spectrally dispersed fluorescence resulting upon excitation with photons in the energy range 12.65–41 eV produced by a synchrotron radiation source. They found five super-excited states, of which the lowest one, at around 14.5 eV, is found to produce CH(A) and CH(B) fragments via neutral dissociation. Thus, CH fluorescence induced by three 266-nm photons (14.0 eV) is consistent

with the findings by Kato et al. The CH(C–X) fluorescence was not observed by Kato et al., most likely due to too low measurement sensitivity at this wavelength (314 nm) since the grating was blazed at 500 nm (no information about the responsivity of the CCD is given) [33].

In studies of SESs of CH$_4$ using intense femtosecond laser pulses of 800-nm wavelength, distinct fluorescence peaks corresponding to CH(A, B, C–X) and a very weak spectral line from H (the Balmer-α line at 656 nm) have been observed. In our work, an investigation of the wavelength range 390–680 nm did not reveal any observable emission from excited hydrogen atoms. The energy threshold for creating H($n = 3$), resulting in the Balmer-α line upon deexcitation to $n = 2$, is 16.5 eV [33], which is greater than the 14.0 eV provided by three 266-nm photons, and this may be the reason why this emission was not observed in our study.

Regarding the other fluorescent species, whose intensity dependencies have been investigated, i.e., NH and CN, see Table 1, they obviously cannot be formed through photodissociation only, but also demands chemical reaction. With the laser wavelength and intensity used in the present work, photodissociation of N$_2$ is unlikely. This suggests that both NH and CN are produced in reactions between molecular nitrogen (N$_2$, N$_2$*, or N$_2^+$) and a fragment from photodissociation of CH$_4$.

3.4 Dependence on methane concentration

Emission spectra were recorded in 13 different mixtures of methane and air, corresponding to fuel equivalence ratios, ϕ, ranging from 0.6 to 1.8. The equivalence ratio is defined as $\phi = \left(n_{CH_4}/n_{O_2}\right)_{actual} / \left(n_{CH_4}/n_{O_2}\right)_{stoichiometric}$, where n_{CH_4} is the number of moles CH$_4$ and n_{O_2} is the number of moles O$_2$. The measurements were taken in free gas flows at room temperature (296 K) and atmospheric pressure. Signal intensity versus methane mole fraction for CH$_4$ Raman scattering (a), CH(A–X) fluorescence (b), CN(B–X) fluorescence (c), and NH(A–X) fluorescence (d), is shown in Fig. 5. The data for each spectral feature has been normalized in that the highest signal intensity has been set to unity. As can be seen, all signals increase with increasing methane mole fraction. The linear fits to the experimental data reveal that all spectral features grow linearly with increasing methane concentration. The slopes of the fitted linear curves are: 3.5 for CH$_4$ Raman (a), 3.1 for CH(A–X) fluorescence (b), 4.0 for CN(B–X) fluorescence $\Delta v = 0$ (c), and 2.5 for NH(A–X) fluorescence (d). Within the experimental uncertainty all fits, except for NH(A–X), i.e., panel (d), cuts through the origin. The offset present on the NH(A–X) signal is mainly due to the fact that this emission line is partly overlapping with a nitrogen emission line, namely N$_2$(C–B).
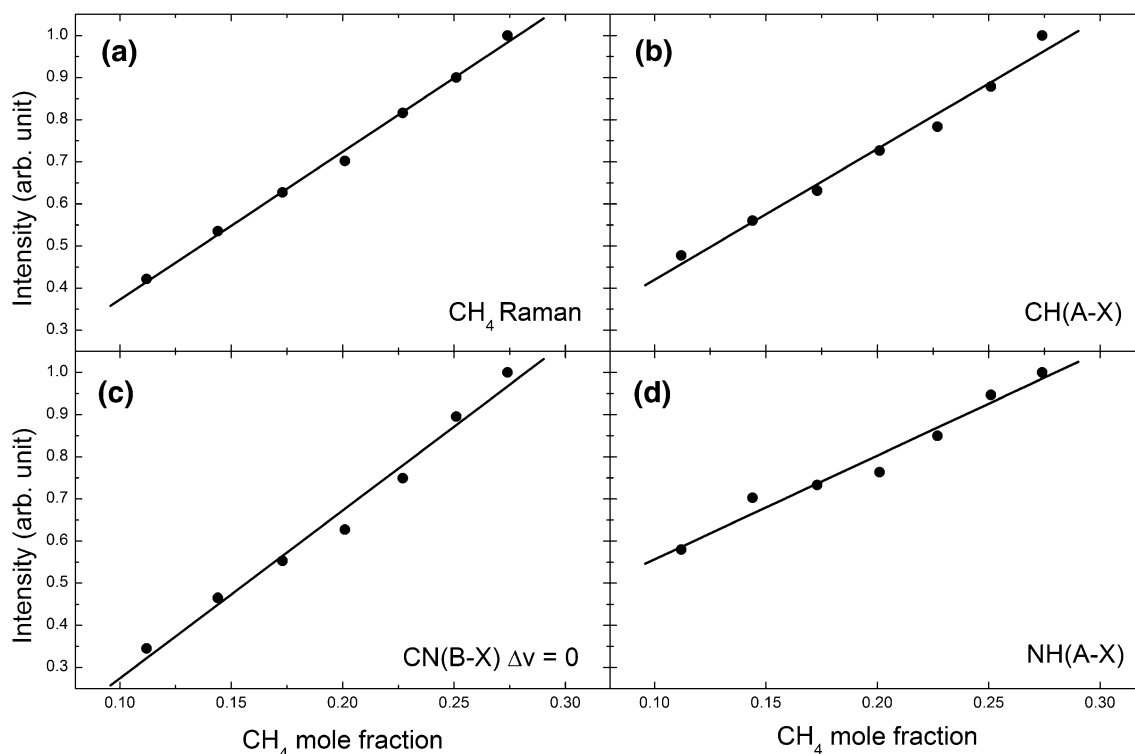
Fig. 5 Signal intensity vs methane mole fraction for the CH_4 Raman scattering (**a**), CH(A–X) fluorescence (**b**), CN(B–X) $\Delta v = 0$ fluorescence (**c**), and NH(A–X) fluorescence (**d**). The *solid lines* are linear fits to the experimental data

Since spontaneous Raman scattering, in contrast to fluorescence, is independent of quenching, predissociation and photoionization, the concentration dependence of the Raman scattering signal of CH_4, i.e., panel (a), can be used as a reference. In other words, a fluorescence signal that depends solely on the methane concentration must have the same slope as the CH_4 Raman signal, i.e., 3.5. The slope for the CH(A–X) signal, i.e., 3.1, is only slightly lower than the slope of the CH_4 Raman signal, indicating that this signal is strongly linked to the methane concentration. Xu et al. have studied the CH(A–X) fluorescence intensity as a function of CH_4 concentration, and they found that the fluorescence signal increases with increasing methane concentration [16]. Given that the methane concentration, in the present study, increases by a factor ~2.5 from the lowest to the highest methane concentration, fluorescence quenching by methane appears to be of minor importance. Hence, this result supports depopulation of CH(A) by 2-photon photoionization, as hypothesized from the laser intensity dependence study discussed in the previous section.

The CN(B–X) fluorescence, shown in panel (c), has a slightly steeper slope than the Raman signal, which could be an indication of decreasing quenching with increasing equivalence ratio. Cross sections for CN(B) quenching have been reported for CH_4, 11.0 Å^2 [12], and for O_2, 25.3 Å^2 [12], while no quantitative

information regarding N_2 quenching was found in the literature. Using these quenching cross sections together with averaged thermal velocities leads to the following quenching rate constants: $k_{CH_4} = 8.75 \times 10^{-11}$ cm^3 s^{-1} and $k_{O_2} = 1.67 \times 10^{-10}$ cm^3 s^{-1}. A situation where the total quenching rate, i.e., $Q = k_{CH_4} \cdot N_{CH_4} + k_{O_2} \cdot N_{O_2} + k_{N_2} \cdot N_{N_2}$ (where N_i is the number density, in molecules/cm^3, of species i), is decreasing with increasing ϕ, would require a nitrogen quenching cross section larger than 10 Å^2. Nitrogen is generally known to be a weak fluorescence quencher, and a cross section larger than 10 Å^2, which is only marginally lower than the CH_4 cross section, seems rather unlikely. Hence, a decreasing quenching with increasing equivalence ratio can therefore not explain the steeper slope of CN(B–X) in comparison with the Raman slope. The linear dependence on CH_4 concentration is however in agreement with previous findings by Kotzagianni et al. who studied the fluorescence intensity variation of the CN(B–X) $\Delta v = 0$ band at different methane/nitrogen/oxygen mixtures [18, 20].

The NH(A–X) fluorescence, shown in panel (d), has a slope of 2.5, i.e., lower than the slope corresponding to the Raman signal (3.5). NH must be formed by a chemical reaction of a nitrogen-containing species and a hydrogen-containing fragment. The current study is based on fuel equivalence ratios ranging from 0.6 to 1.8, i.e., while

the methane concentration is increasing by a factor 2.4 the nitrogen concentration is lowered by 18 %. Hence, the lower slope for NH(A–X) might be an indication of that its formation has a stronger dependence on the nitrogen concentration than the methane concentration.

3.5 Temporal characteristics

In order to shed more light on the formation and consumption of the photofragments, streak camera measurements of spectrally resolved emission were carried out. Figure 6 shows such a streak camera image acquired in a stoichiometric methane/air mixture. The fluorescence from different photofragments as well as the Raman scattering from CH_4 is indicated by arrows in the figure. It is evident that the photofragments are created extremely fast. Although the temporal resolution is limited by the 80-ps duration of the laser pulse, the result shown in Fig. 6 gives some indication of that the fluorescing fragments generally takes ~200 ps longer to be formed than the Raman scattering of methane, a process whose duration is basically set by the period of a molecular vibration, i.e., it is expected to be formed within on the order of 10 fs. Azarm et al. have studied the super-excited state of CH_4, from which CH(A, B, C) fragments are produced (see Fig. 4), and they found its lifetime to be 160 fs [31]. They studied the SES by monitoring the CH(A–X) fluorescence induced by an intense femtosecond pump pulse (800 nm), while a 1338-nm probe pulse, also of femtosecond duration, destroys the SES. By measuring the CH(A–X) fluorescence intensity versus pump-probe delay time, the lifetime of the SES could be determined. Our data, shown in Fig. 6, have too low temporal resolution and the CH(A–X) fluorescence is somewhat obscured by the CN(B–X) $\Delta v = +1$ fluorescence, which prevents an adequate comparison with the result of Azarm et al. [31]. However, it is clear that the more spectrally isolated and more intense CH(C–X) fluorescence is slightly delayed, relative to the CH_4 Raman scattering, and a detailed analysis of the data shown in Fig. 6 shows that the delay is ~200 ps. Despite the limited temporal resolution, our result suggests that neutral dissociation of CH_4, via an SES at 14.0 eV (three 266-nm photons), into a CH(C) fragment takes significantly longer time than dissociation into CH(A) via an SES at 15.0 eV as reported in [31]. As discussed in Sect. 3.2, where it was noted that our measured rotational and vibration temperatures of the CH(C) fragment are significantly higher than those reported in [15], it is possible that CH(C) to some extent is formed by chemical reactions with species originating from N_2 and O_2, which, of course, would impact its formation rate.

Fluorescence lifetimes of the fragments were extracted based on the data from the streak camera image shown in Fig. 6. Due to the generally weak fluorescence signals, only
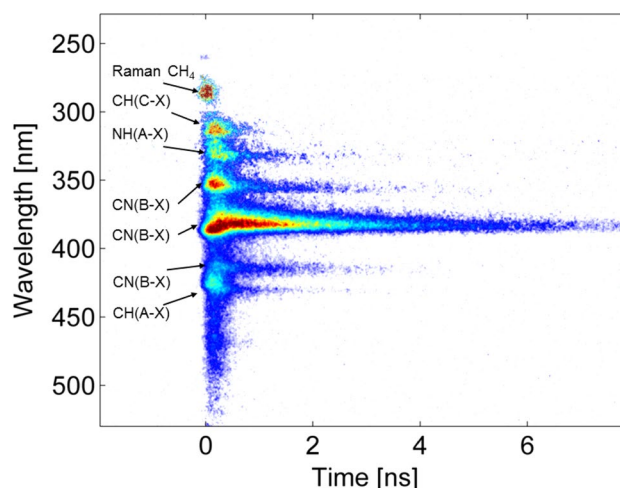

Fig. 6 Spectrally resolved streak camera image (average of 15,000 laser shots) of the emission induced by the picosecond laser in the stoichiometric CH_4/air mixture. Identified photofragments are denoted in the figure

integrated lifetimes, corresponding to all rovibronic transitions within each fluorescence band, were determined, i.e., pixels were binned along the vertical direction across the entire signal from each fragment in Fig. 6. The fluorescence signals were plotted in log-linear diagrams, which revealed that the signals consist of a strong initial component decaying with a constant slope followed by a significantly weaker component having a different, less steep, constant slope, i.e., the fluorescence decays are bi-exponential. This is the case for all signals except for the CN(B–X) $\Delta v = 0$ fluorescence, which shows a single-exponential decay. Since the signals are heavily dominated by their initial parts, only the decay times associated with these parts are reported here, see Table 3. Since the fluorescence tails suffer from low signal-to-noise ratios, reliable decay times from these regions are difficult to extract from the present data. Nevertheless, we have made an attempt to estimate these decay times by making fits to the latter part of the signals, and they were found to be 2.3 ± 0.5 ns for all investigated fluorescence curves.

As can be seen in Table 3, all fluorescence lifetimes, except for CN(B–X) $\Delta v = 0$, are below 1 ns. A calculation based on only collisional quenching by CH_4, N_2, and O_2, using quenching cross sections from [34], for a stoichiometric mixture, results in a lifetime for CH(A–X) fluorescence of 8 ns, which is in agreement with the measured CH lifetime by Xu et al. [17]. This lifetime is ~20 times longer than the measured lifetime. As discussed in Sect. 3.3, the laser intensity dependence suggests that CH(A, B, C) might be depopulated by 2-photon photoionization (see Fig. 4), which could explain the short lifetimes of CH(A) and CH(C).

Table 3 Fluorescence lifetimes determined from the spectrally resolved streak camera image shown in Fig. 6

Spectral feature	Fluorescence lifetime (ns)
CN(B–X) $\Delta v = 0$	2.03 ± 0.01
CN(B–X) $\Delta v = +1$	0.93 ± 0.02
CN(B–X) $\Delta v = -1$	0.54 ± 0.05
CH(C–X)	0.53 ± 0.10
CH(A–X)	0.39 ± 0.03
NH(A–X)	0.74 ± 0.04

Fig. 7 High-resolution streak camera image of the fluorescence signals from CN(B–X) $\Delta v = 0$ and N_2^+(B–X). The image is based on signal accumulated over 30,000 laser shots

The fluorescence lifetime for NH(A–X) was calculated assuming quenching by CH_4, O_2 and N_2 as the only non-radiative deexcitation processes. Quenching rate constants for $v' = 0$ are available for CH_4 and O_2 from Ref. [35]. The quenching rate constants reported in [35] are for low rotational states; $N' = 1$ to 6 for CH_4 and $N' = 1$ to 5 for O_2. Quenching by N_2 was neglected as it is known to have a very low cross section (<0.01 Å^2) from studies at room temperature [36]. For CH_4 and O_2, the average values of the quenching rate constants for the different rotational states were used to calculate the fluorescence lifetime, which was found to be 1.1 ns. This value is about 30 % higher than the measured fluorescence lifetime, i.e., 0.74 ns (see Table 3). As the quenching rate constants decreases with increasing rotational state (N') [35], it may seem surprising that the measured lifetime is shorter than the calculated since the NH(A) state exhibits very high vibrational and rotational temperatures (5000 and 3000 K, respectively, as shown in Table 2). However, the lifetime calculation is based on quenching rate constants from only $v' = 0$, which obviously is a severe limitation as higher vibrational states clearly are populated. The measured NH(A–X) fluorescence lifetime thus suggests that the quenching rate constants are higher in the excited vibrational states than in $v' = 0$.

Figures 1 and 6 clearly illustrate that the CN(B–X) $\Delta v = 0$ is the strongest fluorescence signal in this study. The reason for this is because this fluorescence has the highest Einstein coefficient for spontaneous emission, for the $v' = 0 \rightarrow v'' = 0$ band, which is $A_{00} = 1.36 \times 10^7$ s^{-1} [25] for example. The average values based on four vibrational transitions within each vibrational sequence, i.e., $\Delta v = 0, -1$, and $+1$, are $A_{\Delta v=0} = 1.06 \times 10^7$ s^{-1}, $A_{\Delta v=-1} = 2.99 \times 10^6$ s^{-1}, $A_{\Delta v=+1} = 1.69 \times 10^6$ s^{-1}. Thus, $A_{\Delta v=-1}$ is 28 % of $A_{\Delta v=0}$ and $A_{\Delta v=+1}$ is 16 % of $A_{\Delta v=0}$. As can be seen in Figs. 1 and 6, this trend is reflected in the experimental data. The fluorescence lifetime of CN(B–X) $\Delta v = 0$ is 2.03 ns. This value agrees well with 2.26 ± 0.23 ns, which was measured using time-resolved laser-induced fluorescence (excitation to $v' = 0$) by
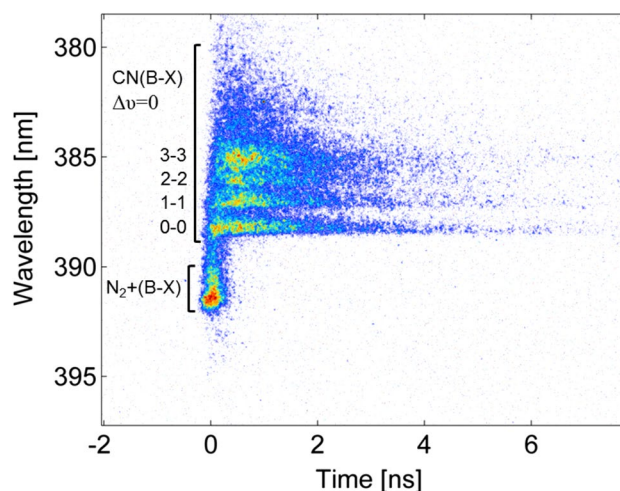
Schwarzwald et al. [37] in a $CH_4/N_2O/N_2$ flame . Schwarzwald et al. [37] also found that the lifetime was rather insensitive to variation in stoichiometry (no significant difference in the range $\phi = 1.02–1.42$) and height above burner. Thus, the CN(B–X) fluorescence lifetime, and thereby the quenching rate, is fairly insensitive to variations in chemical composition and temperature. Therefore, it is not surprising that the $\Delta v = 0$ lifetime measured here agrees well with the lifetime reported in [37], in spite of the fact that the measurements were taken in different chemical compositions and at vastly different temperatures.

The CN(B–X) $\Delta v = 0$ fluorescence was analyzed in greater detail by recording a streak camera image with high spectral resolution. The result is displayed in Fig. 7. In addition to the CN (B–X) $\Delta v = 0$ signal, N_2^+(B–X) fluorescence is visible in the image at around 391 nm. The fluorescence lifetimes corresponding to the 0–0, 1–1, and 2–2 vibrational bands are found to be 2.23 ± 0.01, 2.02 ± 0.01, and 2.04 ± 0.02 ns, respectively. These lifetimes correspond well with the integrated lifetime of 2.03 ns extracted from the low-resolution data shown in Fig. 6. The fact that the variation in lifetimes for the 0–0, 1–1, and 2–2 bands is less than 10 % suggests that the difference in non-radiative depopulation rates of $v' = 0, 1$, and 2 is less than 10 %. The signal-to-noise ratio is not high enough to discern the vibrational bands 3–3, 4–4, etc., but they are hidden in the blurry structure between 380 and 385 nm in Fig. 7. Evaluation of the total signal in this wavelength region results in a fluorescence lifetime of 1.25 ± 0.05 ns, which suggests that the non-radiative deexcitation rates are higher for $v' \geq 3$.

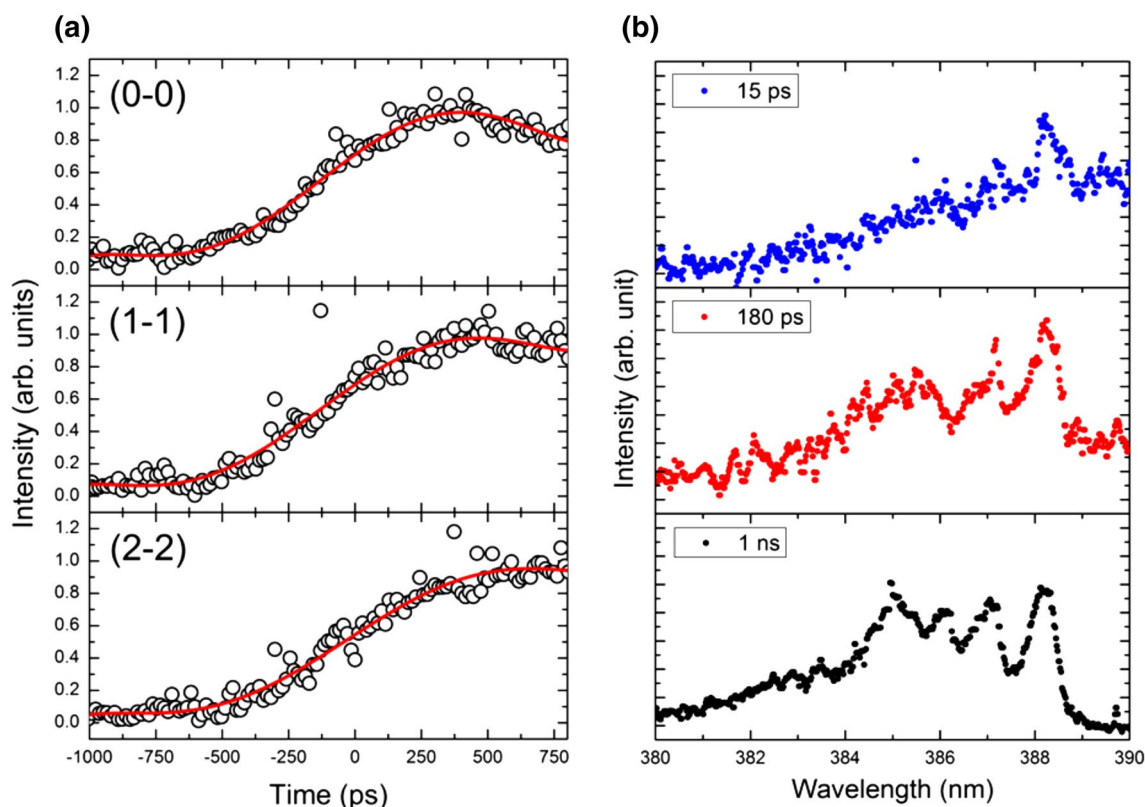It is evident from Fig. 7 that the N_2^+(B–X) fluorescence lifetime is much shorter than the lifetime of CN(B–X)

Fig. 8 a Horizontal cross sections extracted from Fig. 7 illustrating the growth of the three fluorescence bands. The signal corresponding to the 0–0 band is shown in the upper panel, the 1–1 band in the middle panel, and the 2–2 band in the lower panel. The *red solid lines* are fitted third-order polynomials, only serving as a guide for the eye. **b** Fluorescence spectra at three different times, i.e., three vertical cross sections of the signal shown in Fig. 7. The upper spectrum (*blue dots*) corresponds to the population after 15 ps (signal averaged from −55 to 85 ps), the middle spectrum (*red dots*) corresponds to the population after 180 ps (signal averaged from 90 to 260 ps), and the lower spectrum (*black dots*) corresponds to the population after 1.00 ns (signal averaged from 0.260 to 1.76 ns)

$\Delta v = 0$. Unfortunately, the temporal resolution was not sufficiently high to determine its lifetime.

The image shown in Fig. 7 reveals that $v' = 0$ is populated first, while the higher vibrational levels are populated later, with a rate that decreases with increasing v'. This trend is more clearly observable in Fig. 8a, where horizontal cross sections corresponding to the 0–0, 1–1, and 2–2 bands have been extracted from Fig. 7. The three fluorescence bands have reached maximum intensity after the following times: 410 ps (0–0), 450 ps (1–1), and 670 ps (2–2), which means that $k_{v=0}/k_{v=1} = 1.1$ and $k_{v=0}/k_{v=2} = 1.6$, where k_v is the production rate of CN in state v. Hence, the chemical reaction rate is decreasing with increasing vibrational state.

The population dynamics is further shown in Fig. 8b, where three vertical cross sections of the image shown in Fig. 7 are plotted. The cross sections reflects the vibrational population distribution at three different times after the formation of CN(B). The upper spectrum (blue dots) corresponds to the population after 15 ps (signal averaged from −55 to 85 ps), the middle spectrum (red dots) corresponds to the population after 180 ps (signal averaged from 90 to 260 ps), while the lower spectrum (black dots) corresponds to the population after 1.00 ns (signal averaged from 0.260 to 1.76 ns).

4 Significance of the results and diagnostic development

The present study is a detailed investigation of the emission resulting upon strong UV laser illumination of different methane/air mixtures. It is found that a number of luminescent fragments, i.e., CH, CN, NH, OH, and N_2^+, are formed due to photodissociation, photoionization, and photochemical reactions. In fact, fluorescence from these species is observable even for the lowest laser pulse energy investigated, i.e., 0.4 mJ, corresponding to an irradiance of ~30 GW/cm^2. These results constitute crucial information for the application of existing laser diagnostic techniques based on strong UV excitation, which are widely used in for example combustion research, as they show that such

methods, unless the laser intensity is kept low enough, might not be entirely non-intrusive and also hampered by interfering emission from photofragments. Examples of techniques utilizing high UV laser intensities are saturated laser-induced fluorescence (LIF) and multi-photon LIF, which are described and discussed in [38, 39].

Although not claimed to be non-perturbing, since deliberate photodissociation of a target species forms its basis, photofragmentation laser-induced fluorescence (PFLIF) is another method for which the current results are important. The PFLIF method is described in detail in [40], and here we only give a brief description of the concept. The molecule of interest is photodissociated into fragments using a UV laser pulse. Then one of the fragments is probed using a second laser pulse, whose wavelength is tuned to a strong absorption line of the fragment, which results in laser-induced fluorescence. Since the LIF-signal intensity reflects the concentration of photofragments, the method yields an indirect measure of the parent molecule concentration. Photofragmentation laser-induced fluorescence has been used for detection of hydrogen peroxides in flames [41], where OH fragments from UV-photolysis of predominantly HO_2, constitute the signal of interest. In premixed methane/air flames, a photochemical interference, originating from photodissociation of hot CO_2, has been observed and predicted by detailed chemical kinetics modeling. The intensity of the interfering signal decreases with decreasing pump-probe delay time (see Fig. 10 in [41]). Utilization of picosecond pump and probe pulses would allow sub-nanosecond delays, which thus potentially may reduce the interfering signal substantially. The results presented here, however, show that the potential benefits of using picosecond pulses and a sub-nanosecond delay might be inhibited by the production of other interfering signal contributions, in particular the OH(A–X) and CH(C–X) fluorescence as can be seen in Fig. 2a. The lifetime of the CH(C–X) fluorescence is found to be 0.53 ns (see Table 3), while the signal-to-noise of the OH(A–X) fluorescence was not high enough for a reliable determination of its lifetime. The OH fluorescence lifetime is, however, expected to be shorter than 2 ns [42]. Thus, the influence from fluorescence from CH(C–X) and OH(A–X) might be negligible for a pump-probe delay of 2 ns if a detector with a steep gate function, synchronized with the probe laser firing, is used. It should also be noted that the OH signal observed in this work only reflects the presence of electronically excited fragments, i.e., OH(A). It is possible that also ground state fragments, i.e., OH(X), are formed, and these will then add another interfering signal contribution in PFLIF detection of hydrogen peroxides as these fragments will be probed as well.

Despite the potential limitations imposed by strong UV excitation, the present results also suggest that the multitude of luminescent fragments may form the basis for a method measuring the local fuel equivalence ratio, as described in the following section.

4.1 Multivariate analysis for determination of equivalence ratio in methane/air mixtures

To show how picosecond photofragmentation can be used for sensing the equivalence ratio in an unknown mixture of methane and air, multivariate analysis was applied on the 13 normalized emission spectra recorded in different methane/air mixtures. Multivariate analysis using singular value decomposition (SVD) is a technique commonly used in chemometry to reduce large data sets and create predictive models. Intuitively, SVD can be interpreted as a method to investigate where in a data set the most variation occurs by transforming a data set to an orthonormal basis, where the data can be represented by a few principal components. Correlating the variation to known variables gives the possibility to develop a statistical model to predict the values of the variables based on new measurements. For a detailed description of multivariate analysis and the methods used, the reader is referred to [43]. In this work the data set consists of 13 normalized emission spectra recorded at known equivalence ratios between 0.6 and 1.8. The singular values, determining the relative importance of the principal components, are decreasing in significance after the third singular value. Truncation of the model at this point provided a reduced model to accurately determine the equivalence ratio. The first three normalized principal components are seen in the inset of Fig. 9. The model was verified with leave-one-out cross validation (LOOCV), and the result is shown in Fig. 9. In LOOCV a model is created after leaving one of the measurements out and thereafter evaluating the model by calculating what value the left out measurement would give. This is done for every measurement point, and the predicted equivalence ratio is seen to agree very well with the real equivalence ratio, predicting the equivalence ratio within 4 % of the real value. The advantage of SVD compared to intensity-based methods, where the integrated intensity of a spectral band is correlated with the equivalence ratio, is that the SVD is independent of laser energy fluctuations, collection efficiencies, and error sources related to the detected intensity. Singular value decomposition is similar to the ratiometric method, where the ratio of two spectral bands is correlated with the equivalence ratio [20]; however, SVD can be interpreted to have as many spectral bands as pixels in the spectrum, which increases the accuracy of the method drastically. Utilizing this technique on spectrally resolved measurements along a line would allow determination of spatially resolved local equivalence ratios, thus providing a great asset for combustion research.
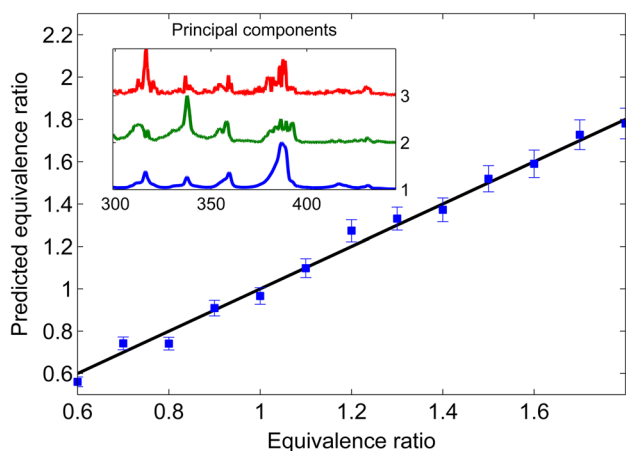
Fig. 9 Predicted equivalence ratios based on singular value decomposition and the leave-one-out cross validation. The solid line represents expected equivalence ratios and blue squares are the predicted values with error bars derived from the standard deviation of all points. *Inset* First three normalized principal components where the number to the right denotes the corresponding principal component. The principal components 2 and 3 show where the biggest variation in the spectrum occurs as a function of equivalence ratio. The x axis of the inset is wavelength

5 Conclusions

This study presents novel results, showing that an intense $(2.0 \pm 0.5) \times 10^{11}$ W/cm^2, 80-picosecond laser pulse at 266-nm can break several chemical bonds in gas mixtures of methane and air at atmospheric pressure and room temperature. Emission spectra are, for the first time, studied with ultrahigh temporal resolution using a streak camera. The main findings are: (a) the focused beam of 266-nm picosecond pulses leads to the formation of several luminescent fragments, namely CH(A$^2\Delta$, B$^2\Sigma^-$, C$^2\Sigma^+$), CN(B$^2\Sigma^+$), NH(A$^3\Pi^-$), OH(A$^2\Sigma^+$) and N$_2^+$(B$^2\Sigma_u^+$), i.e., all neutral species except N$_2^+$, (b) all neutral fragments are created with very high vibrational and rotational temperatures (2000–8000 K), (c) CH(A, B, C) might be formed through neutral dissociation via a super-excited state of CH$_4$, reached by 3-photon excitation and that 2-photon ionization/dissociation, rather than collisional quenching, dominates the deactivation of these fragments, (d) all fragments observed are created within 200 ps, (e) the fluorescence lifetimes are shorter than 1 ns for all observed transitions except for the $\Delta v = 0$ band of CN(B–X), which is found to be 2.0 ns, and (f) the rate of the chemical reaction that forms CN(B) is decreasing with increasing vibrational state of the product. In addition to providing basic understanding, the results also constitute crucial information for the application of laser diagnostic techniques based on strong UV excitation, as they show that such methods might not be entirely non-intrusive and suffering from spectral interferences due to emissive photofragments, unless the laser intensity is kept sufficiently low. Finally, a novel diagnostic concept, based on multivariate analysis using singular value decomposition, is demonstrated for determination of equivalence ratio. The method is expected to be a useful diagnostic for measurement of local equivalence ratios in for example combustion environments.

References

1. E. Schreiber, *Ultrafast Photodissociation* (Springer, Berlin, 1998)
2. P. Hering, C. Cornaggia, Phys. Rev. A **57**, 4572–4580 (1998)
3. D. Mathur, C. P. Safvan, G. Ravindra Kumar, and M. Krishnamurthy, Phys. Rev. A **50**, R7–R9 (1994)
4. M. Sharifi, F. Kong, S.L. Chin, H. Mineo, Y. Dyakov, A.M. Mebel, S.D. Chao, M. Hayashi, S.H. Lin, J. Chem. Phys. **111**, 9405–9416 (2007)
5. D. Mathur, F.A. Rajgara, J. Chem. Phys. **120**, 5616–5623 (2004)
6. S. Wang, X. Tang, L. Gao, M.E. Elshakre, F. Kong, J. Phys. Chem. A **107**, 6123–6129 (2003)
7. C. Wu, H. Ren, T. Liu, R. Ma, H. Yang, H. Jiang, Q. Gong, J. Phys. B: Atm. Mol. Opt. Phys. **35**, 2575 (2002)
8. J.S. Levine, *The Photochemistry of Atmospheres* (Academic, New York, 1985)
9. R.P. Wayne, *Chemistry of Atmospheres* (Oxford University, New York, 1991)
10. H. Rodhe, Science **248**, 1217–1219 (1990)
11. C. Johnson, J. Henshaw, G. McLnnes, Nature **355**, 69–71 (1992)
12. H.O.W.M. Jackson, *Photodissociation Dynamics of Small Molecules in Advances in Photochemistry*, vol. 13 (Wiley, Colorado, 1986)
13. R. Schinke, *Photodissociation Dynamics* (Cambridge University Press, Cambridge, 1993)
14. R. Schinke, in Encyclopedia of Computational Chemistry (John Wiley & Sons, Ltd, 2002)
15. F. Kong, Q. Luo, H. Xu, M. Sharifi, D. Song, S.L. Chin, J. Chem. Phys. **125**, 133320 (2006)
16. H.L. Xu, J.F. Daigle, Q. Luo, S.L. Chin, Appl. Phys. B. **82**, 655–658 (2006)
17. H.L. Xu, Y. Kamali, C. Marceau, P.T. Simard, W. Liu, J. Bernhardt, G. Méjean, P. Mathieu, G. Roy, J.-R. Simard, S.L. Chin, Appl. Phys. Lett. **90**, 101106 (2007)
18. M. Kotzagianni, S. Couris, Appl. Phys. Lett. **100**, 264104 (2012)
19. H.-L. Li, H.-L. Xu, B.-S. Yang, Q.-D. Chen, T. Zhang, H.-B. Sun, Opt. Lett. **38**, 1250–1252 (2013)
20. M. Kotzagianni, S. Couris, Chem. Phys. Lett. **561–562**, 36–41 (2013)
21. W. Chu, H. Li, J. Ni, B. Zeng, J. Yao, H. Zhang, G. Li, C. Jing, H. Xie, H. Xu, K. Yamanouchi, Y. Cheng, Appl. Phys. Lett. **104**, 091106 (2014)
22. D.W. Hahn, N. Omenetto, Appl. Spectrosc. **64**, 335A–366A (2010)
23. D.W. Hahn, N. Omenetto, Appl. Spectrosc. **66**, 347–419 (2012)

24. S. L. Chin, *Femtosecond Laser Filamentation, Springer series on Atomic, Optical, and Plasma Physics* (Springer Sci. Business Media, New York, 2010), Vol. 55
25. J. Luque, D. R. Crosley, in *LIFBASE: Database and spectral simulation (version 1.5)* (SRI International Report MP 99-009, 1999)
26. C. M. Western, in *PGOPHER, A program for simulating rotational structure (*(University of Bristol, Bristol, UK). http://pgopher.chm.bris.ac.uk, 2010)
27. R.S. Ram, P.F. Bernath, J. Mol. Spectrosc. **260**, 115–119 (2010)
28. S. Yuan, T. Wang, P. Lu, S. Leang Chin, and H. Zeng, **104**, 091113 (2014)
29. K. Liu, D. Song, F. Kong, Laser Phys. **19**, 1640–1650 (2009)
30. A.J.R. Heck, R.N. Zare, D.W. Chandler, J. Chem. Phys. **104**, 4019–4030 (1996)
31. A. Azarm, H. Xu, Y. Kamali, J. Bernhardt, D. Song, A. Xia, Y. Teranishi, S. Lin, F. Kong, S. Chin, J. Phys. B: At. Mol. Opt. Phys. **41**, 225601 (2008)
32. S. G. Lias, J. E. Bartmess, J. F. Liebman, J. L. Holmes, R. D. Levin, and W. G. Mallard, (NIST Standard Reference Database Number 69, http://webbook.nist.gov, retrieved November 29, 2014)
33. M. Kato, K. Kameta, T. Odagiri, N. Kouchi, Y. Hatano, J. Phys. B. **35**, 4383 (2002)
34. M. Tamura, P.A. Berg, J.E. Harrington, J. Luque, J.B. Jeffries, G.P. Smith, D.R. Crosley, Combust. Flame **114**, 502–514 (1998)
35. N.L. Garland, D.R. Crosley, J. Chem. Phys. **90**, 3566–3573 (1989)
36. A. Hofzumahaus, F. Stuhl, J. Chem. Phys. **82**, 3152–3159 (1985)
37. R. Schwarzwald, P. Monkhouse, J. Wolfrum, Symp. (Int.) Combust. **22**, 1413–1420 (1989)
38. A.C. Eckbreth, *Laser diagnostics for combustion temperature and species* (Gordon and Breach Publishers, Combustion science and technology book series, 1996)
39. K. Kohse-Höinghaus, J.B. Jeffries, *Applied Combustion Diagnostics* (Combustion, An international series. Taylor and Francis, 2002)
40. O. Johansson, J. Bood, M. Aldén, U. Lindblad **62**, 66–72 (2008)
41. O. Johansson, J. Bood, B. Li, A. Ehn, Z.S. Li, Z.W. Sun, M. Jonsson, A.A. Konnov, M. Aldén **158**, 1908–1919 (2011)
42. M. Jonsson, A. Ehn, M. Christensen, M. Aldén, J. Bood, Appl. Phys. B. **115**, 35–43 (2014)
43. H. Mark, and J. Workman Jr, *Chemometrics in spectroscopy* (Academic Press, 2010)